

Modeling Time-Intensity Profiles for Pulmonary Nodules in MR Images

Li Shen, Wei Zheng, Ling Gao, Heng Huang, Fillia Makedon, and Justin Pearlman

Abstract—Perfusion magnetic resonance imaging (pMRI) is an important tool to assess tumor angiogenesis for the early detection of lung cancer. This paper presents a novel integrated framework for spatio-temporal modeling of pulmonary nodules in pMRI image sequences. After localizing a nodule region in each image, we perform segmentation in the region to extract nodule boundary, and then use thin-plate spline interpolation for nodule registration along the temporal dimension. The resulting spatio-temporal model can lead to many types of nodule characterization. Time intensity profiles of nodules region capture important angiogenic patterns in the lung that can distinguish between cancer and benign nodules and help early detection.

I. INTRODUCTION

Lung cancer is among the most commonly occurring malignancies in the world and is the leading cause of cancer death in both men and women in the US. Computed tomography (CT) can identify suspicious lesions, but its high false-positive rate often requires additional imaging tests within 3-6 months to confirm a positive result. To detect lung cancer at an earlier stage, an alternative and promising method is to apply perfusion magnetic resonance imaging (pMRI) [1] modified to assess tumor angiogenesis. Angiogenesis is one of the most promising areas in cancer research. It is defined as the formation and development of new blood vessels, essential for tumor growth and the eventual spread of cancer cells to secondary locations throughout the body.

One key issue in the analysis of pMRI lung image sequences is to effectively characterize angiogenic patterns of pulmonary nodules. To achieve this goal, we present a novel and automated spatio-temporal modeling technique for pulmonary nodules in pMRI sequences, and demonstrate our approach by creating a time intensity profile for any user-interested nodule region. Many techniques of nodule detection (*e.g.*, [2]) and segmentation (*e.g.*, [3]) have been developed based on chest radiographs or CT images. New challenges arising in our analysis include the following: (1) as a different imaging modality, pMRI requires new processing techniques for detection and segmentation of lung nodules, and (2) to compensate for respiratory and cardiovascular motion in pMRI sequences, registration needs

to be done to ensure the corresponding nodule occurrences in different time frames to be comparable.

In this paper, a novel integrated framework is presented for spatio-temporal modeling of pulmonary nodules in pMRI image sequences. After localizing a nodule region in each image, we perform segmentation in the region to extract nodule boundary, and then use thin-plate spline interpolation for nodule registration along the temporal dimension. The resulting spatio-temporal model can lead to many types of nodule characterization, *e.g.*, a time intensity profile of a nodule region; and be used to capture important angiogenic patterns in the lung that can distinguish between cancer and benign nodules and help early detection. We describe our method in Section II, present sample results in Section III, and conclude the paper in Section IV.

II. METHODOLOGY

We first describe the image data used in this study, next present our overall strategy, and then discuss each processing step in details. These processing steps include identification, segmentation, and registration.

A. Image Data

Prior written consent was obtained as approved by the hospital research board. Surface EKG electrodes were used for cardiac cycle timing during the MR imaging procedure. MR imaging was performed using an eight-channel phased-array coil of a 1.5-T whole-body GE dual gradient Excite magnet. After scout images of the chest a bolus Fast Gradient-Echo Train imaging (FGRET) was performed at the rate of one image per heartbeat with flip angle adjusted to null the target lesion on fourth and subsequent frames prior to arrival of contrast agent (TR/TE/flip angle = 6.06 ms/1.108 ms/75°, views per segment = 4, matrix = 256 × 256, field of view = 440 × 440 mm, EKG triggered RR = 1). Likewise, static inversion recovery images were adjusted to null the target lesion, typically using TI = 250-300 msec. While imaging by FGRET, 20 ml of Gd-DTPA (Magnevist, Berlex Laboratories) was injected into the venous line as a time series of 80-84 images were obtained at one frame per heartbeat observing signal changes relating to arrival and washout of the contrast agent. Subsequently, at 5, 10, and 15 minutes after injection, delayed enhancement static inversion recovery images were obtained to assess agent retention (which occurs in damaged cells). In this study, we analyze the time series of images obtained during the first-pass of the bolus of contrast agent to demonstrate our spatio-temporal modeling technique. Fig. 1 shows four examples from one series of 84 images.

L. Shen is with the Department of Computer and Information Science, University of Massachusetts Dartmouth, 285 Old Westport Rd, N. Dartmouth, MA 02747, USA (Phone 508 910 6691, Fax 508 999 9144, lshen@umassd.edu)

W. Zheng, H. Huang, and F. Makedon are with the Department of Computer Science, Dartmouth College, Hanover, NH 03755, USA ({wei.zheng, heng.huang, fillia.makedon}@dartmouth.edu)

L. Gao and J. Pearlman are with the Departments of Radiology and Cardiology, Dartmouth Medical School, Lebanon, NH 03756, USA ({ling.gao, justin.pearlman}@dartmouth.edu)

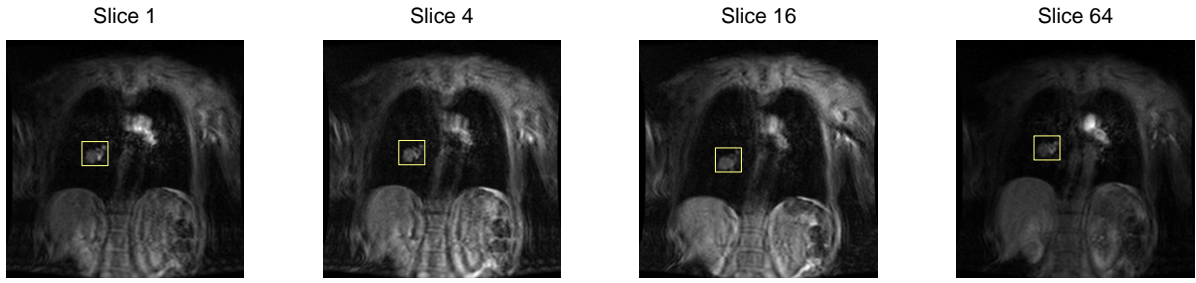


Fig. 1. Nodule region identification. In each slice, the rectangular box indicates the identified nodule region.

B. Overall Strategy

Our overall strategy is to divide the problem into several relatively simple subproblems. Generally speaking, image registration [4] is a difficult task. However, if we localize relevant nodule region that is actually our focus, registration of this sub-image between different time frames becomes a much easier task. More conveniently, we can even extract the nodule boundary from this sub-image, and then use the segmentation results to complete nodule registration. Thus, our framework includes 3 steps: (1) nodule identification in each slice, (2) nodule segmentation in the relevant region, and (3) nodule registration using segmentation results. The following subsections describe these steps in more details.

C. Identification

To identify a local nodule region in each image slice, we employ a simple method as follows. In one slice, we manually define a rectangular region A to enclose the nodule of interest. In other words, A is an $m \times n$ sub-image that contains the nodule.

In each of the other slices, we search for a region B of the same size that maximizes the correlation coefficient between A and B . The two-dimensional correlation coefficient between two matrices A and B of the same size is given by the formula

$$r = \frac{\sum_m \sum_n (A_{mn} - \bar{A})(B_{mn} - \bar{B})}{\sqrt{(\sum_m \sum_n (A_{mn} - \bar{A})^2)(\sum_m \sum_n (B_{mn} - \bar{B})^2)}},$$

where \bar{X} denotes the mean of the elements of matrix X .

In our implementation, after initializing B to have the same location as A , we move B in the neighborhood area, calculate the correlation coefficient for each case, and then select the best one. Although this is a simple approach, it works perfectly on our data. The nodule region is correctly identified in all the slices. Fig. 1 shows four sample image slices with identified nodule regions.

D. Segmentation

Nodule segmentation is performed on each sub-image identified in the previous step, which reduces the complexity of segmentation. Fig. 4 shows sample nodule sub-images, and the nodule appearance in these sub-images is relatively clear. Thus, a few simple image processing techniques can be combined to complete the segmentation task.

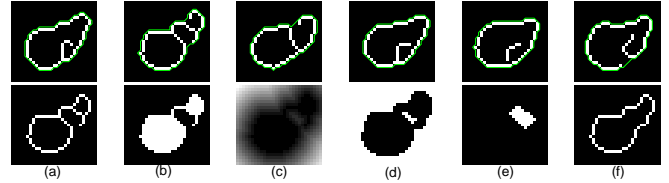


Fig. 2. Nodule boundary segmentation. The first row shows sample edge detection results (white pixels) and segmentation results (green contours). The second row shows a sample procedure of closing broken edges: (a) initial edges, (b) bridge unconnected pixels and fill image region, (c) distance transformation map (DTM), (d) threshold DTM and find connected components, (e) remove the background component and slightly dilate the rest of the components, and (f) extract the boundary of (b)+(e).

We first design a segmentation procedure as follows: (1) Apply a filter to reduce contribution of noise, e.g., 3×3 average, median, or median-average filter (average used in our experiments); (2) apply canny edge detection to extract object edges; (3) if necessary, close the object edges to form a simply-connected object, using an approach described in the next paragraph. The Canny method used in the second step finds edges by looking for local maxima of the gradient of the image. The gradient is calculated using the derivative of a Gaussian filter. The method uses two thresholds, to detect strong and weak edges, and includes the weak edges in the output only if they are connected to strong edges. This method is known to many as the optimal edge detector.

The first row of Fig. 2 shows six sample results after performing the first two steps of the segmentation procedure. Some of these results (a, d and e) form a closed nodule region, while others (b, c and f) do not. The third step is designed as follows to derive a closed nodule boundary: (a) start from the edge detection result; (b) bridge previously unconnected pixels (works only for small gaps) and then fill image regions; (c) calculate the distance transformation map; (d) threshold the transformation map ($t = 1.5$ in our experiments) and find its connected components; (e) remove the background component and slightly dilate the rest components (a radius=3 disk used as the morphological structuring element in our experiments); and (f) add the results of (b) and (e) and extract its boundary. The second row of Fig. 2 shows a sample run of the above procedure.

The above segmentation procedure works for most of nodule sub-images. However, for some noisy cases, it fails to

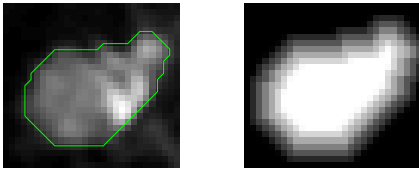


Fig. 3. Mean nodule image (left), mean nodule boundary (green contour), and weighting mask (right).

create a reasonable nodule shape. To overcome this problem, we introduce a weighting mask to capture a general nodule shape and then apply it to each image to impose some structural constraint on the segmentation results.

We use the following approach to calculate the weighting mask: (1) scale the intensity values to the range from 0 (black) to 1 (white) for each sub-image, and calculate the mean image; (2) segment the mean using the procedure described above; (3) calculate the signed distance transformation map of the mean boundary; and (4) threshold the transformation map so that the most positive and negative values become t and $-t$ respectively.

Fig. 3 shows the mean nodule boundary and the weighting mask ($t = 3$ in this case). Since the weighting mask captures a general nodule shape, we multiply it to each nodule image on a pixel-by-pixel basis and then perform segmentation as described before. Clearly, this approach imposes structural constraint on each individual nodule so that its shape won't deviate too much away from a typical nodule shape. Using this strategy, we obtain satisfactory results for all the images. Fig. 4 shows some of the results (see blue stars).

E. Registration

After segmentation, the spatial characteristics of a nodule are available at each time point. To build a spatio-temporal nodule model, we need to complete the registration along the temporal dimension. In other words, for each pixel inside the nodule in a user-specified slice, we need to find its corresponding pixels in all the other slices. We develop a landmark-based registration approach, which includes automatic identification of landmarks in each slice and thin-plate spline interpolation [5] for image matching.

A landmark is a point of correspondence on each nodule occurrence that matches between time frames. We develop the following procedure to automatically extract a set of landmarks in each slice. We run principal component analysis (PCA) [6] to each nodule represented by a binary image to find its principal axes. These principal axes intersect the nodule boundary at four points, which become our base landmarks. We can then extract more landmarks by finding the midpoint of the contour between two neighboring landmarks and defining it as a new landmark. Besides these boundary landmarks, we also include the nodule centroid as an additional landmark. In our experiments, we use 32 boundary landmarks and 1 centroid landmark. Fig. 4 shows the PCA axes and sample landmarks. These are labeled landmarks, which are consistent across subjects.

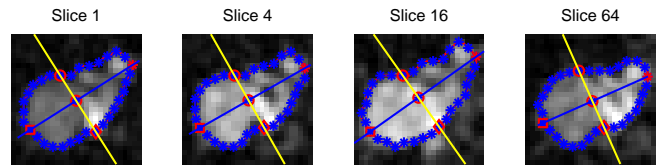


Fig. 4. Principal axes and landmarks (consistent across subjects). Image intensity is scaled for better visualization.

Landmarks define the correspondence at the nodule boundary and centroid. To create correspondence for the interior part, we employ thin-plate spline interpolation [5]. A thin-plate spline $f(x, y)$ is a smooth function which interpolates a surface that is fixed at the landmark points P_i at a specific height h_i . If one imagines this surface as a thin metal plate, then this plate will take a shape in which it is least bent, *i.e.*, it minimizes the bending energy of $f(x, y)$:

$$\int \int_{R^2} \left(\frac{\partial^2 f}{\partial x^2} \right)^2 + \left(\frac{\partial^2 f}{\partial x \partial y} \right)^2 + \left(\frac{\partial^2 f}{\partial y^2} \right)^2 dx dy.$$

In order to map one image to another using landmark data, we compute two of these spline surfaces, one (f_x) in which the heights (h_i 's) are loaded with the x -coordinate of the landmarks (P_i 's) in the second image, another (f_y) for the y -coordinate. Then the first of these functions supplies the interpolated x -coordinate of the map we seek, and the second the interpolated y -coordinate. The resulting map ($f_x(P)$, $f_y(P)$) is now a deformation of one image plane onto the other which maps landmarks onto their homologues and has the minimum bending energy of any such interpolant.

Fig. 5 shows sample results of applying thin-plate spline interpolation to our data. Clearly, given any nodule pixel in the first slice, now we can find the corresponding pixels in all the other slices. This completes our discussion of nodule registration across different time frames.

III. RESULTS

We demonstrate our spatio-temporal modeling technique using the pMRI image sequence shown before, which comprises 84 lung perfusion, short-axis, MR images obtained from one freely breathing patient. We apply our identification, segmentation, and registration algorithms to these images, and Figures 1, 4 and 5 show sample results at different stages. After these steps, a spatio-temporal model has been established for the nodule of interest, a cancer nodule in this case.

Using this model, we can create a time intensity profile for a region of interest (ROI) in the nodule. Such an ROI can be specified in any slice. According to our model, the corresponding ROI in all the other slices can be easily extracted. Thus a time intensity profile for the ROI could be created as a curve showing mean intensity (or intensity variance) change over time.

This profile in relation to an upstream arterial profile defines the point-spread function for blood delivery to the observed loci, which is largely determined by the convolution effects from small pathways (angiogenesis). In particular,

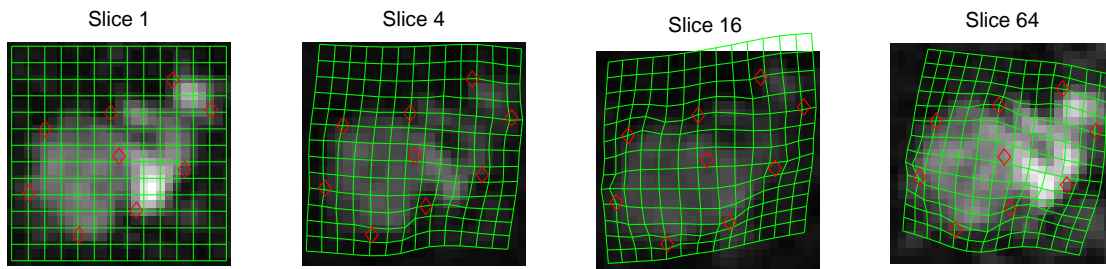


Fig. 5. Thin plate spline interpolation. The registration results are visualized by meshes. The image intensity is not scaled.

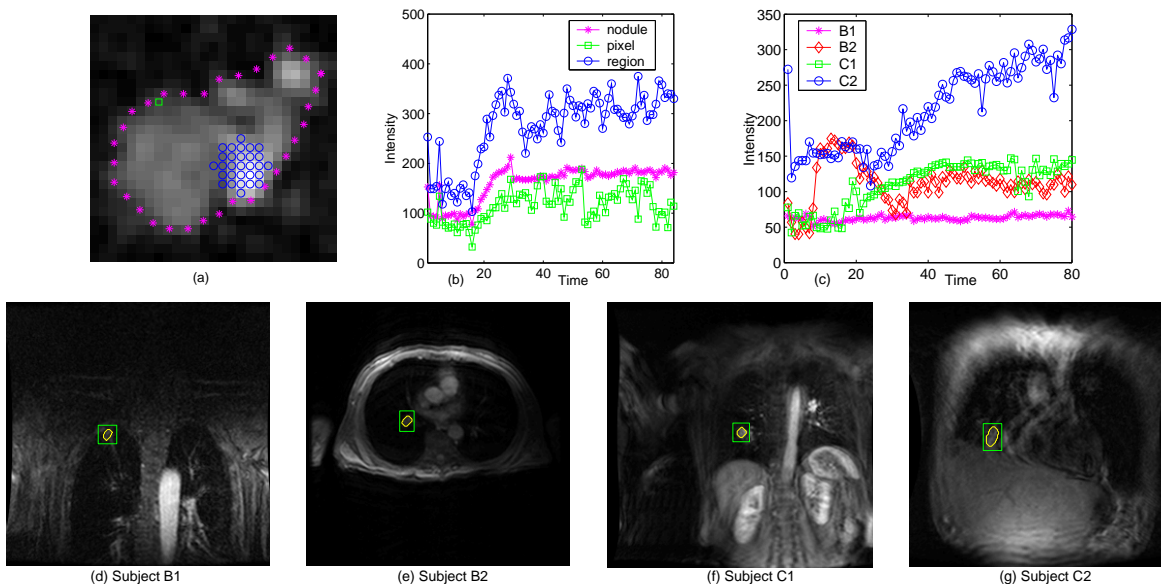


Fig. 6. (a) Three ROIs defined on a cancer nodule: a single pixel (green square), the whole nodule (bounded by pink stars), and a region (blue circles). (b) Time intensity profiles of the ROIs in (a). (c-g) Lung images with nodules of interest for two benign cases (d-e) and two cancer cases (f-g), and time intensity profiles of these four nodules (c), where the green box identifies the nodule location and the yellow contour defines the nodule boundary.

if the blood delivery pattern is consistent with increased microvascular development, that implicates tumor angiogenesis, and timing with respect to pulmonary vein enhancement helps distinguish primary lung cancers from metastases.

Fig. 6(a-b) shows several ROIs defined for the nodule in the above sequence and their profiles by plotting the mean intensity versus the time. We have also done experiments for a few other image sequences and the results are shown in Fig. 6(c-g): (d-e) two benign nodules, (f-g) two cancer ones, and (c) their time intensity profiles. These time intensity profiles can capture different types of angiogenic patterns of the pulmonary nodule and have a potential in distinguishing cancer nodules from benign ones. Work is in progress to collect and process more cases in order to achieve this goal.

IV. CONCLUSIONS

We have presented an integrated framework for spatio-temporal modeling of pulmonary nodules in pMRI image sequences, and demonstrated its application in creating time intensity profiles for any user-interested nodule regions. This spatio-temporal model can also lead to many other types of nodule characterization, e.g., volume/shape change over

time. One future direction is to use this model to extract important angiogenic patterns in the lung that can lead to effective discrimination between cancer and benign nodules and help early accurate detection of lung cancer.

V. ACKNOWLEDGMENTS

This work was supported by the Flight Attendant Medical Research Institute.

REFERENCES

- [1] C. Fink, M. Puderbach, *et al.*, "Regional lung perfusion: assessment with partially parallel three-dimensional MR imaging," *Radiology*, vol. 231, no. 1, pp. 175–84, 2004.
- [2] Y. Lee, T. Hara, H. Fujita, *et al.*, "Automated detection of pulmonary nodules in helical CT images based on an improved template-matching technique," *IEEE Trans. on Medical Imaging*, vol. 20, pp. 595–604, 2001.
- [3] N. Xu *et al.*, "Automated lung nodule segmentation using dynamic programming and EM based classification," in *SPIE Medical Imaging*, vol. 4684-70, 2002.
- [4] J. Maintz and M. Viergever, "A survey of medical image registration," *Medical Image Analysis*, vol. 2, pp. 1–36, 1998.
- [5] F. Bookstein, "Principal warps: Thin-plate splines and the decomposition of deformations," *IEEE Trans. on Pat. Ana. and Mac. Int.*, vol. 11, no. 6, pp. 567–585, 1989.
- [6] R. O. Duda, P. E. Hart, and D. G. Stork, *Pattern Classification (2nd ed)*. New York, NY: Wiley, 2000.